2 Chemistry

2-1 XAFS Study of HZSM-5-Supported N-Interstitial Re-Cluster Catalysts for Direct Phenol Synthesis with Benzene and Molecular Oxygen

Phenol is one of the most important chemicals in industrial processes, but is currently produced from benzene with three-step cumeme processes, producing lots of by-products. Direct synthesis from benzene using molecular oxygen is an alternative way to overcome the energy problems but no selective catalyst with good performance has yet been found in an economically and environmentally favorable benzene-O_2 system. We have succeeded in the preparation of HZSM-5-supported Re catalysts by chemical-vapor deposition of methyltrioxorhenium and found that the supported Re catalysts exhibited high phenol selectivity (88% for steady-state reaction and 94% for pulse reaction) for direct phenol synthesis from benzene and O_2 in the presence of NH_3 [1]. These phenol selectivities are the highest values ever reported for direct phenol synthesis from benzene and O_2. The structures of the supported Re species were studied using Re L-edge XAFS, and it was found that the NH_3 produced Re_{10} clusters, which are the active species for the catalytic phenol synthesis.

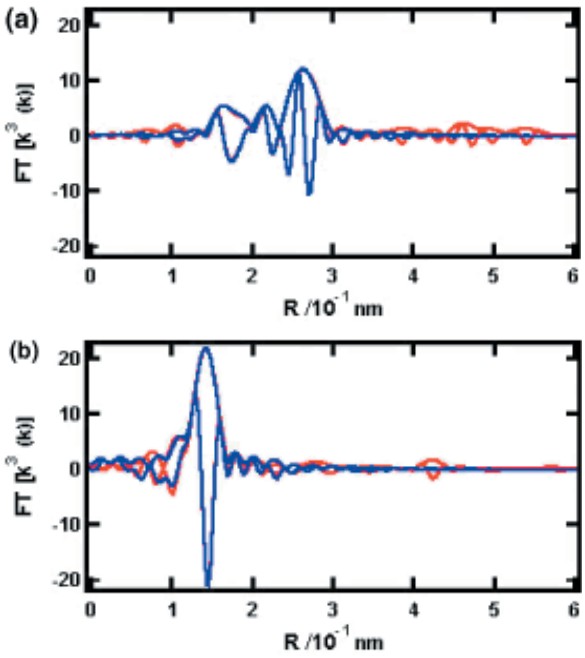

Figure 1
Fourier transforms of Re L_3-edge EXAFS spectra recorded at 15 K for (a) the NH_3-treated Re-cluster catalyst on HZSM-5 and (b) the Re monomer following pulse reaction with benzene and O_2. Red: observed. Blue: fitted.

The Re catalyst prepared on HZSM-5 (SiO_2/Al_2O_3=19) exhibited the highest phenol selectivity in the presence of NH_3, while there was no phenol formation in the absence of NH_3. The rate of phenol formation decreased in the following order: HZSM-5(SiO_2/Al_2O_3=19) > HZSM-5(23.8) > HZSM-5(39.4) >> H-Mordenite > H-beta > H-USY. NH_3 was essential for phenol production, but excessive NH_3 decreased the activity by undesirable poisoning. No positive effects were observed using H_2O and N_2O, and with other basic compounds such as pyridine and isopropyl amine the phenol formation did not proceed at all.

EXAFS studies at the Re L_3 edge showed the nature of the active species for phenol synthesis. Fourier transforms of the spectra are presented in Fig. 1. NH_3 treatment with the HZSM-5-supported Re catalyst caused a structural transformation to Re clusters with Re-Re bonds at a distance of 0.276 nm (Fig. 1 (a)). The treatment with NH_3 reduces the oxidation state of Re to the lower valence state, as also suggested by XANES and XPS studies. Density-functional-theory(DFT) calculations based on the structural parameters revealed by EXAFS (CN(Re-Re)=5.2, CN(Re-N)=2.8, CN(Re=O)=0.3) showed that the structure of the active Re species is Re_{10} clusters composed of two shared-edge octahedral Re_6 frameworks (Fig. 2). Pulsing both benzene and O_2 on the NH_3-pretreated Re_{10} clusters produced phenol efficiently. While the NH_3-pretreated catalyst did not produce phenol with pulsing only of the benzene, indicating that the lattice oxygen of the Re_{10} clusters was not involved in the selective oxidation. These results demonstrate that the Re_{10} clusters are the active species and that molecular oxygen is necessary for phenol formation.

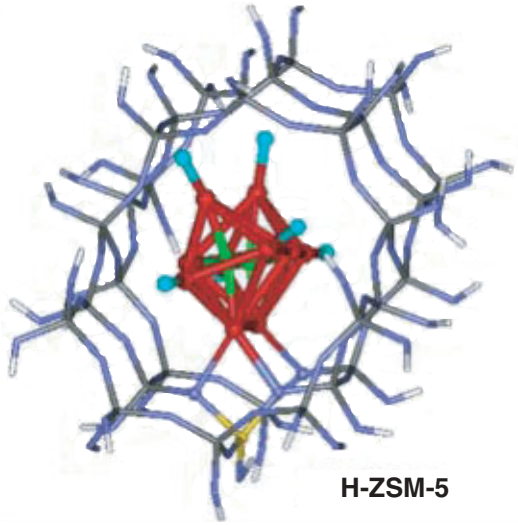

Figure 2
Proposed structure of the supported Re-cluster catalyst on HZSM-5 obtained using DFT calculations.

In the pulsed experiments, the phenol formation rate dropped to zero after 4 pulses. Thus the coexistence of NH_3 is essential for phenol synthesis, and Re_{10} clusters are not stable under O_2 in the absence of NH_3. The Re_{10} clusters were transformed to Re monomers as proved by EXAFS (Fig. 1 (b)). The presence of oxygen molecules not only promotes phenol formation, but also has the undesirable effect of converting Re_{10} clusters to monomers. During steady-state reaction in the presence of NH_3, about 3-4% of the Re monomers are estimated to be transformed to active Re_{10} clusters responsible for the formation of phenol.

M. Tada and Y. Iwasawa (The Univ. of Tokyo)

References

[1] R. Bal, M. Tada, T. Sasaki and Y. Iwasawa, *Angew. Chem. Int. Ed.* (Selected as HOT PAPER), **45** (2006) 448.

2-2 *In-Situ* XAFS Study of a Ni_2P Catalyst under Hydrodesulfurization Conditions – Development of a New XAFS Measurement Technique for High Pressure and High Temperature Gas-Liquid Phase Reactions –

Recently hydrodesulfurization (HDS) has attracted great attention due to severe legislation world-wide limiting the amount of sulfur in transportation fuels. The improvement of HDS catalysts is now of great importance. However, because of the difficulties in atomic-level resolution analysis of liquid phase reactions, the structural study of HDS catalysts is usually performed under gas-phase model conditions rather than practical liquid phase conditions. Since XAFS is feasible even in the liquid phase, considerable effort has been made in the design of suitable experimental cells for XAFS [1,2]. However, the cells developed to date have the drawbacks either of using toxic beryllium as X-ray windows or of having tubular shapes which distort the XAFS spectra due to differences in sample thickness.

In this work, these problems have been solved by the development of a low-volume cell with flat cubic boron nitride (c-BN) windows (Fig. 3) [3]. High purity c-BN is a material that has only recently become available. It is transparent to X-rays and stable chemically, mechanically and thermally. Moreover, its tensile strength is 1079 MPa, second only to the tensile strength of 2000 MPa of diamond. It has no tendency to form cracks even at 1473 K.

XAFS measurements of catalysts under liquid-phase HDS catalytic-reaction conditions at high pressure and high temperature have been performed at BL-9C. To our knowledge, this is the first example of *in-situ* XAFS measurements of HDS catalysts under practical conditions. The catalyst studied in this work is a novel material, Ni_2P/SiO_2, which shows extremely high activity for HDS and hydrodenitrogenation with better performance than commercial sulfide catalysts [4,5]. The catalyst was activated in the cell at 723 K under H_2, and *in-situ* XAFS measurements were performed under reaction conditions. Figure 4(a) shows an *in-situ* EXAFS oscillation measured at 613 K and 3 MPa under H_2 just before the initiation of the reaction. Figure 4(b) shows the oscillations under steady-state reaction conditions at 613 K and 3 MPa of H_2 under a model oil feed composed of 20 wt% tetralin and 77 wt% tetradecane with 3 wt% dibenzothiophene. Since Ni_2P consists of clusters with diameters of ca. 6 nm and only about 15% of the Ni atoms are located in the surface region, structural changes limited to the surface are hardly distinguishable in the observed spectra. Taking a difference spectrum between the spectra recorded before and during the reaction reveals a small but distinctive oscillations (Fig. 4(c)). The lack of any systematic distortion in the background indicates that the subtraction was successful. Curve fitting simulations assuming a Ni-S bond give a good fit at a distance of 0.228 ± 0.004 nm. Although an XRD analysis of Ni_2P/SiO_2 before and after the reaction gave only one phase, Ni_2P, for the bulk structure of the supported Ni species, the difference EXAFS spectrum reveals that the surface

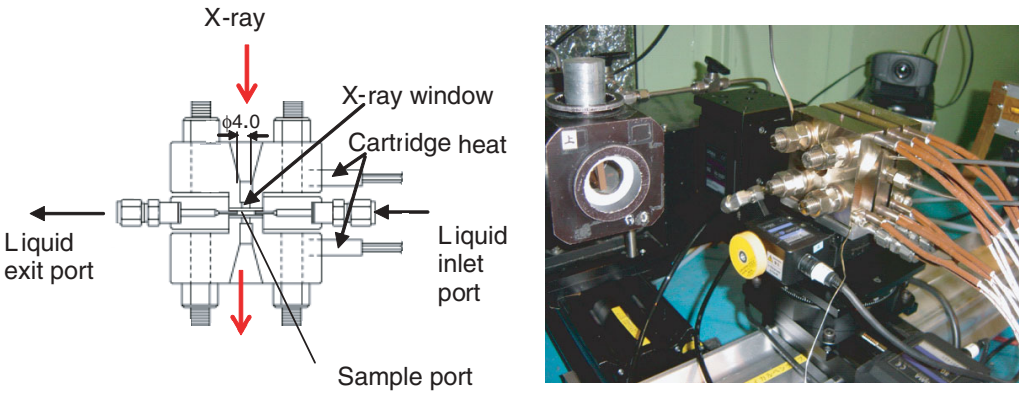

Figure 3
Top view of the *in-situ* EXAFS cell (left) and a photograph of the cell attached to the beam line (right).

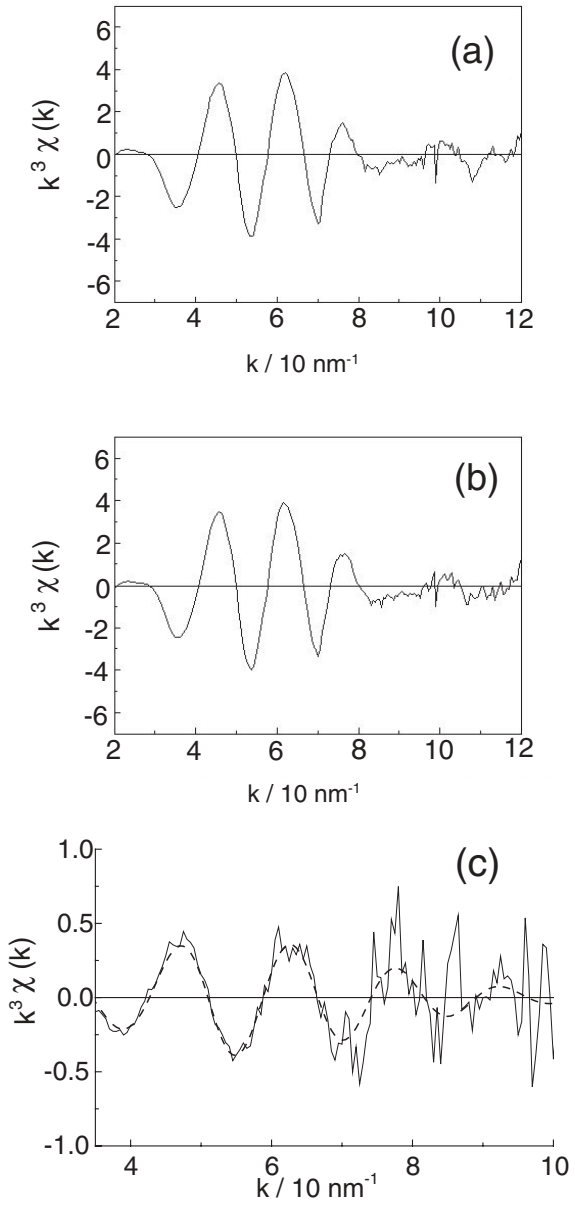

Figure 4
EXAFS oscillations $k^3\chi(k)$ for SiO_2-supported Ni_2P just before the feed flow (a) and 10 hours after the reaction initation (b) under steady state conditions (613 K, 3 MPa). (c) The difference between (a) and (b) is depicted as a solid curve in (c). The dotted curve corresponds to that calculated for a Ni-S bond using FEFF.

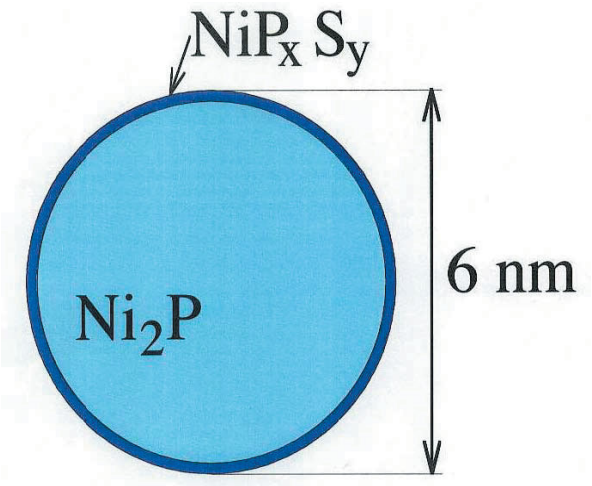

Figure 5
Proposed structure of active Ni species.

of Ni_2P was partially sulfided in the course of the HDS reaction. It is concluded therefore that the surface phosphosulfide species is in the active phase (Fig. 5).

The direct subtraction method described here is only applicable to *in-situ* EXAFS spectra of the catalyst because the measurement temperature can be kept constant and the change in the X-ray beam spot position is negligibly small.

The technique developed in this work is available for the study of other catalytic systems which require severe reaction conditions.

T. Kawai[1], K. K. Bando[2], Y. -K. Lee[3], S. T. Oyama[3], W. -J. Chun[1] and K. Asakura[1] ([1]Hokkaido Univ., [2]AIST, [3]Virginia Polytech. Univ.)

References

[1] J. -D. Grunwaldt, M. Ramin, M. Rohr, A. Michailovski, G. R. Patzke and A. Baiker, *Rev. Sci. Instrum.*, **76** (2005) 054104.
[2] N. Weiher, E. Bus, B. Gorzolnik, M. Möller, R. Prins and J. A. van Bokhoven, *J. Synchrotron Rad.*, **12** (2005) 675.
[3] T. Kawai, K. K. Bando, Y. -K. Lee, S. T. Oyama, W. -J. Chun and K. Asakura, *J. Catal.*, **241** (2006) 20.
[4] S. T. Oyama, *J. Catal.*, **216** (2003) 343.
[5] S. T. Oyama, X. Wang, Y. -K. Lee and W. -J. Chun, *J. Catal.*, **221** (2004) 263.

2-3 A Study of the Accumulation Mechanism in Arsenic Hyperaccumulator Fern, *Pteris vittata* L. Using XAFS and XRF Imaging Techniques

The arsenic hyperaccumulator plant, Chinese brake fern (*Pteris vittata* L.), can contain extremely high level of arsenic (*ca.* 20000 μg g^{-1} dry weight) when grown on contaminated soil [1]. This plant is now put to commercial use as part of phytoremediation technology, which uses plants to remove hazardous substances from the environment. Chemical forms of arsenic have been intensively studied for clarifying the accumulation mechanism of arsenic in the fern [2]. On the other hand, the arsenic distribution has been investigated only in individual plant organs such as the pinnae or stems, and its distribution is still unclear at the cellular and subcellular levels. The conventional SEM-EDS mapping technique is not suitable for this purpose because of the low sensitivity of electron-beam excitation for the analysis of heavy elements such as arsenic. Although a renovated SEM with a cooling stage under a low vacuum is suitable for obtaining clear three-dimensional images of plant cells, information on the elemental distribution at the cell level cannot be obtained using SEM-EDS and the arsenic accumulation mechanism has not fully been elucidated.

We have recently utilized synchrotron radiation

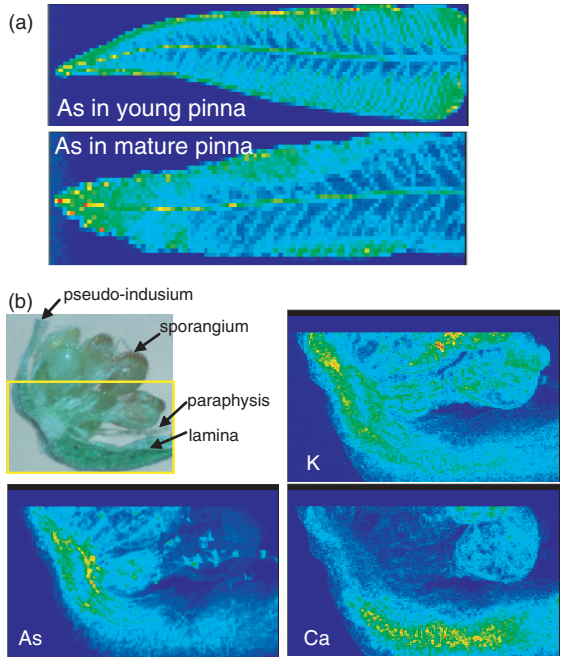

Figure 6
Elemental distribution in the pinna of *Pteris vittata* L.
(a) Arsenic distributions in young and mature pinnae. Beam size: 200 × 200 μm^2.
(b) Elemental distribution in the edge of the pinna. Beam size: 3.5 × 5.5 μm^2.

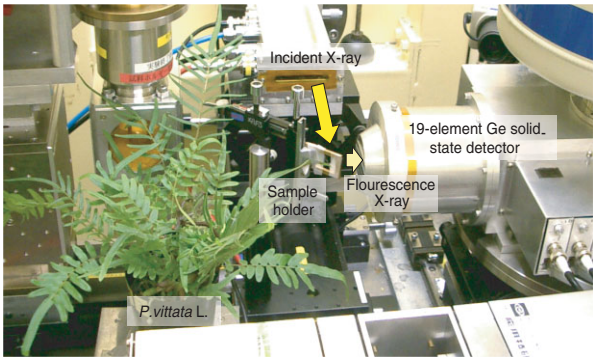

Figure 7
A photograph of *in vivo* measurement of the As K-XANES spectrum of a fern grown in a pot at PF BL-12C.

μ-XRF (X-ray fluorescence) analysis to elucidate the arsenic distribution in the arsenic hyper-accumulating fern [3]. A focused microbeam (3.5 × 5.5 μm^2) produced by Kirkpatrick-Baez mirror at BL-4A was used to determine the elemental distribution in the tissue and cells of fern. Fronds of various ages were studied. The arsenic distribution in the pinnae of the fronds was found to change with varying growth stage. The results indicated that high levels of arsenic accumulate at the base of sporangium in the lamina of the pinnae (Fig. 6). The living fern was also investigated using X-ray Absorption Near Edge Structure (XANES) analysis in the fluorescence mode without any sample treatment in order to elucidate the arsenic oxidation state (Fig. 7). It was found that arsenic exists in the As(III) form in the pinnae, and as a mixture of As(III) and As(V) in the rachis, though As(V)

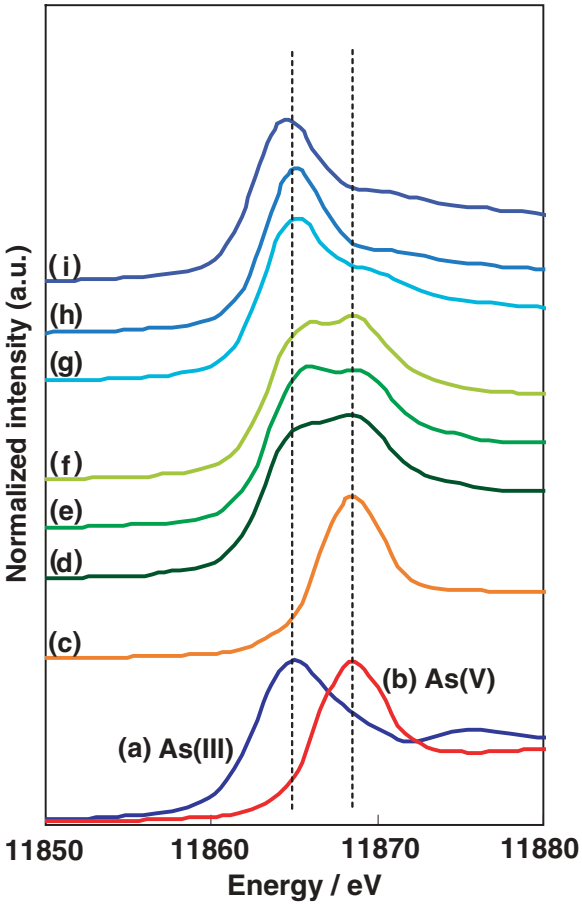

Figure 8
Normalized arsenic K-edge XANES spectra. The spectra were normalized to the maximum ratio of fluorescence intensity (I_f) to incident intensity (I_0); (a) and (b) are the reference materials As_2O_3 and H_3AsO_4, (c) cultured soil contaminated with arsenic, (d)-(i) mature frond samples analyzed non-destructively. (d) petiole, (e) middle midrib, (f) upper midrib, (g) base of pinna, (h) apex of pinna, (i) edge of pinna with spore. (g)-(i) were collected from one pinna at the apex position on the frond.

was dominant in the cultivated soil (Fig. 8). These findings indicate that the fern takes up arsenic in the As(V) form from the soil and that the As(V) is then partially reduced to As(III) within the plant. Finally arsenic accumulates as As(III) in a specific area of the pinna. This is the first report demonstrating that arsenic is accumulated in a specific tissue in the pinna.

A. Hokura[1], R. Onuma[1], T. Kashiwabara[1], N. Fukuda[1], N. Kitajima[1,2] and I. Nakai[1] ([1]Tokyo Univ. of Science [2]Fujita Co.)

References

[1] L. Q. Ma, K. M. Komar, C. Tu, W. Zhang, Y. Cai and E. D. Kennelley, *Nature*, **409** (2001) 579.
[2] S. M. Webb, J. -F. Gaillard, L. Q. Ma and C. Tu, *Environ. Sci. Technol.*, **37** (2003) 754.
[3] A. Hokura, R. Onuma, Y. Terada, N. Kitajima, T. Abe, H. Saito, S. Yoshida and I. Nakai, *J. Anal. At. Spectrom.*, **21** (2006) 321.

2-4 XAFS Analyses of Ni Species Trapped in Carbon Nanofibers

Carbon nanofibers (CNFs) and carbon nanotubes (CNTs) have applications such as electric devices, hydrogen reservoirs and medical usage. Metal catalysts such as Ni play an important role in their synthesis process. However, it is a serious problem that a small amount (~100 ppm) of Ni impurity remains in the CNFs/CNTs following Ni-removal treatment in current preparation procedures, since this residual Ni is toxic for the living body. Therefore, information on the structure and chemical state of residual Ni species is important for developing medical applications of CNFs/CNTs.

Recently, Asakura *et al*. reported K-edge XAFS spectra of Ni species in CNF before and after Ni removal treatment recorded at BL-9A [1]. The XANES spectrum before treatment is quite similar to that of Ni foil, whereas a clearly different spectrum was observed after treatment, with two characteristic peaks appearing in the absorption edge region.

The EXAFS analyses give us one-dimensional information on coordination numbers and distances. In addition, detailed XANES analyses with multiple-scattering calculations can provide us with information on the three-dimensional stereochemical structure around the X-ray absorbing atom. The main purpose of this study is to understand the electronic and geometric structure around Ni impurities in CNF following removal treatment by applying full multiple-scattering XANES analyses [2].

We have considered many possible models for the structure following treatment [3]. Figure 9 shows the observed data along with calculations based on best-fitted model structures. In model (a), one carbon atom is replaced with a Ni atom in the CNF (monomer model), whereas in (b) two carbon atoms are replaced with two Ni atoms (dimer model). Although the calculated first peak (at 7 eV as measured from the onset of K-edge absorption) is a little weaker than the experimental one, the calculated spectra using both models reproduce the two specific peaks observed in the absorption edge region. By comparing the two models, the spectrum of the dimer model gives a smaller peak at 7 eV and a rapid decrease above 30 eV as compared to the monomer model. Other models such as carbide or diamond structures do not reproduce well the observed data. We thus conclude that following removal treatment, most of the Ni impurities in CNF have the monomer structure.

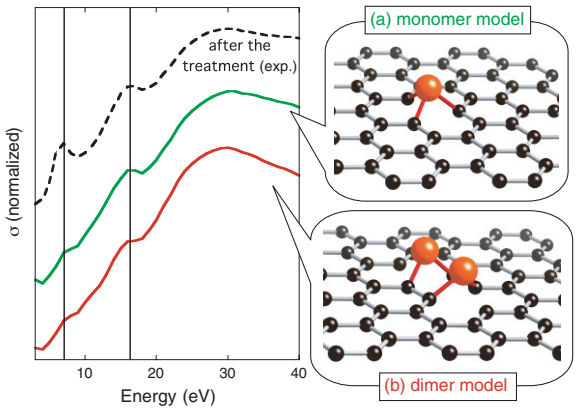

Figure 9
Comparison of the calculated Ni K-edge XANES spectra for the monomer model (a) and the dimer model (b) with the spectrum observed following treatment. In (a), a Ni atom binds to three carbon atoms in the graphene sheet, and in (b), two Ni atoms bind to two nearby carbon atoms in the sheet. The energy scale is relative to the onset of the K-edge absorption.

We have further analyzed how the curvature of CNTs affects the XANES spectra by the use of multiple scattering theory. We consider two models (Figs. 10(a) and (b)). In the 'inside model', a Ni atom is located inside the tube (Fig. 10(a)), while in the 'outside model' a Ni atom is outside the tube (Fig. 10(b)). Figure 10 shows the calculated XANES spectra for these two CNT models, and we can clearly see differences between them. So far no experimental results to be compared with our calculations are available, but our molecular orbital analyses support the 'outside model' [4]. Further experimental XANES measurements on Ni/CNT could shed light on which model is correct. The difference may arise from the different distances from the second-nearest carbon atoms. In the XANES region, the mean free path is rather large and the stereochemical difference further than the first shell is reflected in the spectra through multiple scatterings. Our results demonstrate that it may be possible to distinguish between Ni atoms located inside and outside the tube.

A XAFS analysis combined with multiple-scattering calculations is a powerful tool for characterizing the nano-structures of species present in small amounts.

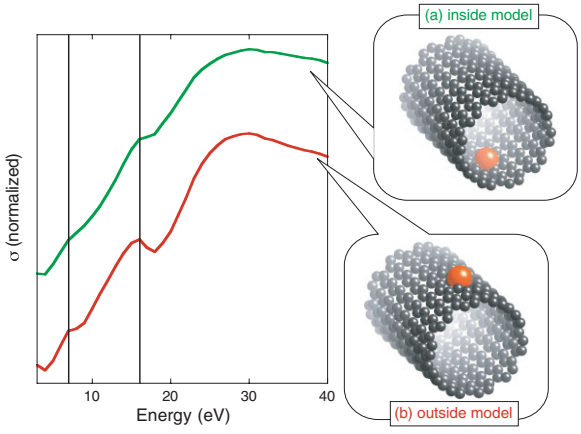

Figure 10
Calculated XANES spectra for the two CNT models. In model (a) the single Ni atom is located inside the tube, and in model (b) it is located outside the tube.

M. Ushiro[1], K. Uno[1], S. Nagamatsu[1], Y. Sato[2], K. Tohji[2], F. Watari[3], W. J. Chun[3,4], Y. Koike[3], K. Asakura[3] and T. Fujikawa[1] ([1]Chiba Univ., [2]Tohoku Univ., [3]Hokkaido Univ., [4]JST-CREST)

References

[1] K. Asakura, W. J. Chun, K. Tohji, Y. Sato and F. Watari, *Chem. Lett.*, **34** (2005) 382.
[2] T. Fujikawa, *J. Phys. Soc. Jpn.*, **62** (1993) 2155.
[3] M. Ushiro, K. Uno, Y. Sato, K. Tohji, F. Watari, W. J. Chun, Y. Koike, K. Asakura and T. Fujikawa, *Phys. Rev. B,* **73** (2006) 144103.
[4] M. Ushiro, K. Asakura, K. Ohminami, S. Nagamatsu and T. Fujikawa, *e-J. Surf. Sci. Nanotech.*, **3** (2005) 427.

2-5 Reverse Conformational Changes of a Lever-Arm Drive Directional Motility of the Myosin V and Myosin VI Processive Motors

The molecular mechanism of protein motors, by which the chemical free energy of ATP hydrolysis is transduced with high efficiency to power intra-cellular transport (see Fig. 11A), is a major area of active investigation in biological science. Myosin, one of the motor proteins, moves on the actin filaments and constitutes a superfamily. Class V myosin (myosin V) and class VI myosin (myosin VI) are newly found "unconventional" myosins. Both these myosins contain two globular motor core domains and long tail helices (often called lever-arms). They move processively on actin filaments for long distances without dissociating and carry the cellular trafficking cargo in different directions. Myosin V, like most myosin motors exemplified by skeletal muscle myosin (myosin II), moves toward the plus end of the actin filament, whereas myosin VI moves toward the minus end (Fig. 11B). In order to clarify the underlying mechanism of the directional motility on the actin filament, we have used X-ray solution-scattering techniques to investigate the nucleotide-dependent conformational changes of the subfragment-1 (S1) of myosin V and myosin VI processive motors that govern this directional preference.

Recombinant myosin V-S1 with two IQ motifs (MV-S1IQ2) and myosin VI-S1 (MVI-S1) were protein-engineered from Sf9 cells using a baculovirus expression system. The X-ray solution-scattering experiments were carried out at BL-15A using the small-angle diffractometer, and the scattering data were recorded with a one-dimensional position-sensitive detector. The radii of gyration (Rg) were deduced from the slopes of Guinier plots of the scattering curves in the small-angle region. Figure 12 shows the Rg values of MV-S1IQ2 and MVI-S1 constructs in various nucleotide-bound states as functions of protein concentration [1]. The Rg values extrapolated to zero concentration of nucleotide-free MV-S1IQ2 and MVI-S1 were 48.6 Å and 48.8 Å, respectively, very similar to the value of skeletal myosin II-S1 in a nucleotide-free state. Changes in the extrapolated Rg value for the MgATP solution differed for the two constructs; the Rg

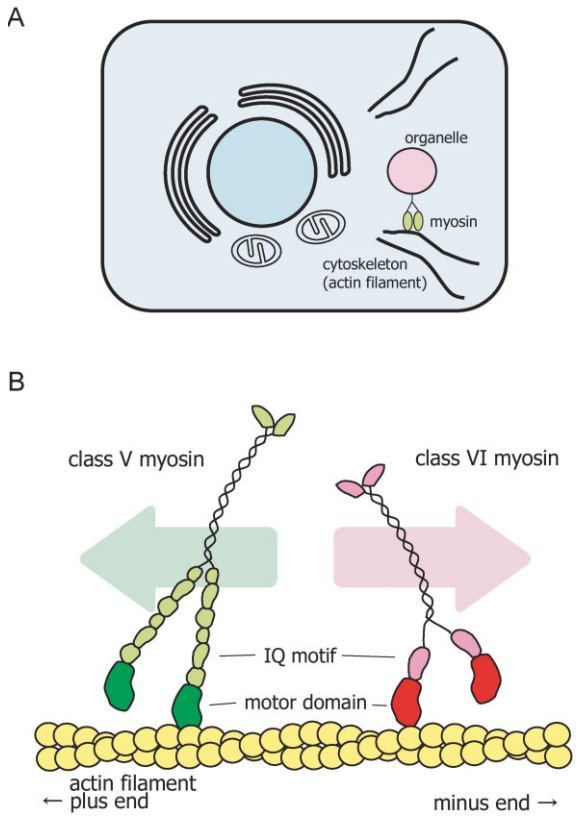

Figure 11
Intra-cellular transport of cargo by a myosin motor protein (A). Schematic drawing of the motility of two-headed myosin, myosin V and myosin VI, on the actin filament (B). Class V myosin contains a motor domain (shown in green) and six IQ motifs (light green); class VI myosin consists of a motor domain (red) and a single IQ motif (pink).

value of MV-S1IQ2 decreased to 46.7 Å while that of MVI-S1 increased to 51.7 Å. These opposite changes in Rg show that opposing directional conformation changes occur in the two myosin S1s, since the change in Rg represents a global conformation change of the lever-arm element of S1 [2,3]. To certify the shape changes of these molecules in MgATP solution, we carried out modeling studies using an *ab initio* algorithm developed by Svergun and colleagues, constructing the three-dimensional shape of a molecule from the one-dimensional scattering profile. These results are depicted in Fig. 13 [4]. The models of MV-S1IQ2 in the presence and absence of ATP show that the molecular shape becomes compact in ATP by swinging its lever-arm portion, very similar to the behaviour of skeletal muscle myosin II-S1 [2]. By contrast, the models of MVI-S1 reveal that the shape becomes more elongated in ATP solution by moving the lever-arm in opposite direction. Our results indicate that MVI-S1 in MgATP solution positions its lever-arm in the opposite direction to MV-S1IQ2 and myosin II-S1, suggesting that the directional preference of myosin motility along actin filaments is closely associated with directional alterations of the lever-arm element during hydrolysis of ATP. As shown in Fig. 12, the binding of a non-hydrolysable ATP analog, AMPPNP, induced Rg changes of these constructs similar to those in ATP, suggesting that the force-producing conforma-

tional changes in these myosins occur on the binding of ATP, and not in a transition state (ADP and phosphate-bound state) as is the case for conventional myosin motors during the cycle of ATP hydrolysis. This timing of the structural changes that drive the directed motility may be characteristic of the processive myosin motors. After the release of phosphate and ADP, the orientation of the lever-arms returned through the slightly different dispositions in the ADP-bound state.

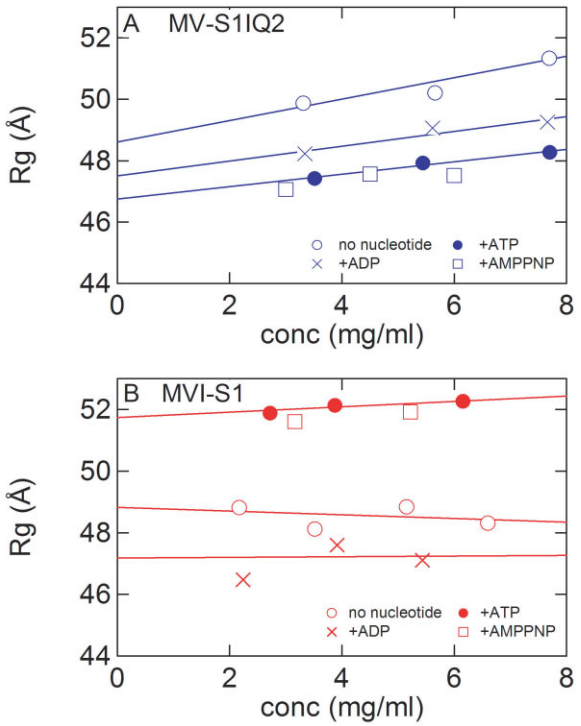

Figure 12
Protein concentration dependence of the radius of gyration (Rg) derived from the Guinier plots of the small-angle scattering data for myosin V-S1IQ2 and myosin VI-S1constructs in various nucleotide-bound states. (A) MV-S1IQ2 construct, (B) MVI-S1 construct.

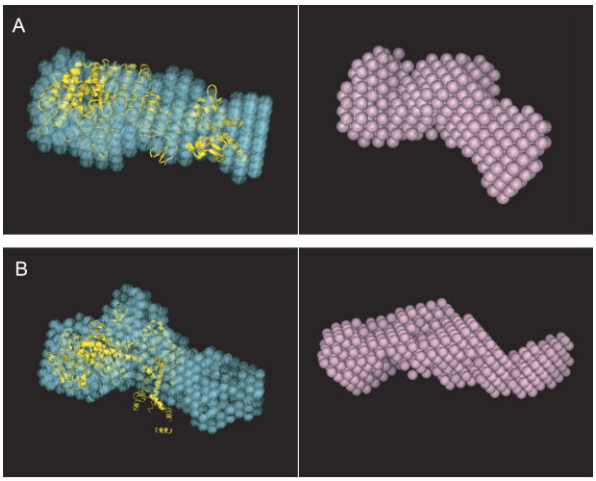

Figure 13
Models of myosin V-S1IQ2 and myosin VI-S1 constructs reconstructed using the *ab initio* shape prediction algorithm. (A) Models of MV-S1IQ2 in the absence (left, blue) and presence (right, pink) of MgATP. (B) Models of MVI-S1 in the absence (left, blue) and presence (right, pink) of MgATP. Partial crystal structures of MV-S1 (pdp:1QE9) and MVI-S1 (pdp:2BK1) are superimposed on each model without MgATP.

Y. Sugimoto[1], O. Sato[2], S. Watanabe[2], K. Wakabayashi[1] and M. Ikebe[2] ([1]Osaka Univ., [2]Univ. of Massachusetts Med. Sch.)

References

[1] Y. Sugimoto, O. Sato, S. Watanabe, M. Ikebe, Y. Takezawa and K. Wakabayashi, *Photon Factory Activity Report*, **22B** (2004) 245.
[2] Y. Sugimoto, M. Tokunaga, Y. Takezawa, M. Ikebe and K. Wakabayashi, *Biophys. J.*, **68** (1994) 29.
[3] J. Higo, Y. Sugimoto, K. Wakabayashi and H. Nakamura, *J. Comput. Chem.*, **22** (2001) 1983.
[4] Y. Sugimoto, O. Sato, S. Watanabe, M. Ikebe and K. Wakabayashi, *Photon Factory Activity Rept.*, **23B** (2005) 235.

2-6 Small-Angle X-Ray Scattering Study of the Pulley Effect of Slide-Ring Gels

Slide-ring (SR) gel [1] is a new type of gel synthesized by cross-linking cyclodextrins (CDs) sparsely distributed in polyrotaxanes in solutions. A polymer network of SR gel is topologically connected by figure-of-eight cross-links of CDs. SR gels have attracted much attention due to their characteristics, and show great potential for many applications, such as biomaterials, cosmetics, and soft actuators. One of the remarkable characteristics displayed by SR gel is the “pulley effect”, whereby the polymer chains freely pass through the cross-links, which act as pulleys. When the gel is stretched, structural homogeneity on the nano-scale is assumed, and stress is equalized due to the pulley effect.

It is widely known that the scattering pattern of stretched gel shows a characteristic anisotropic pattern, the so-called “abnormal butterfly pattern” [2]. This pattern is attributed to the anisotropy of the nanoscopic inhomogeneity within the structure that is induced by the elongation of polymeric materials. This inhomogeneity is introduced during the gelation process. The small-angle scattering patterns of many stretched gels show the abnormal butterfly pattern. The small-angle neutron scattering observed in stretched SR gels [3] is not of the abnormal but “normal” butterfly pattern. The normal butterfly pattern is elliptical with the long axis perpendicular to the stretching direction. This suggests that the nanoscopic inhomogeneity of SR gels is remarkably different from that of chemical gels.

We have investigated the structure of SR gels in various solvents using small-angle X-ray scattering (SAXS), comparing our results to those for chemical gels. The SAXS results for SR gels showed that in a poor solvent where the sliding cross-links form aggregates, the pulley effect is prevented from working, while the polymer chains freely pass through the cross-links acting as pulleys in a good solvent with no aggregation of cross-links. Figure 14 shows the SAXS patterns of acrylamide

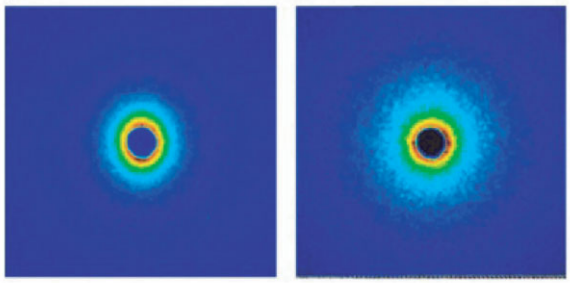

Figure 14
SAXS patterns of (a) stretched AAm gels and (b) stretched SR gels in a good solvent. The sample is elongated in the horizontal direction of the images, and the stretching ratio, ε, is 1.5.

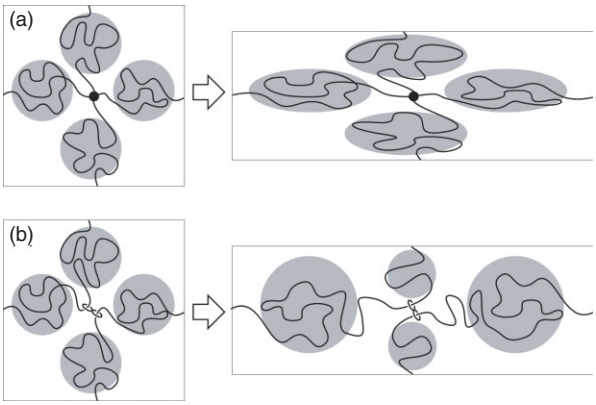

Figure 15
Schematic model of the structural change in (a) chemically bonded gels and (b) SR gels in a good solvent under elongation.

(AAm) gels and SR hydrogels in a good solvent. The gels were stretched horizontally with a stretching ratio ε =1.5. The SAXS patterns show no anisotropy for the SR gels, whereas they exhibit an elliptic pattern with the long axis perpendicular to the stretching direction (ellipticity ~ 1.2) for the AAm gels. This indicates that the polymer chains are deformed by the elongation. The vertically elliptic pattern is due to the horizontally elongated polymer chains.

This difference can be explained by the following model (Fig. 15). In the AAm gel, the cross-links are covalently bonded and can resist the deformation. Thus, the polymer chains connecting in the direction parallel to the elongation are stretched parallel to the elongation axis, while those connecting the cross-links vertically are compressed in the direction perpendicular to the elongation axis. Thus, the polymers are deformed as shown in Fig. 15 (a), leading to a vertically elliptic SAXS pattern. On the other hand, the polymer chains of the SR gel freely pass through the cross-links due to the pulley effect when the gel is stretched. The tension at the horizontally stretched parts and vertically compressed parts of polymers can be equilibrated by an interchange of the chains passing through the cross-links to maximize entropy. Thus the polymers of the SR gel in a good solvent maintain an isotropic structure even under elongation, a result quite different from the behaviour seen in chemical gels.

Y. Shinohara, K. Kayashima, Y. Okumura, C. Zhao, K. Ito, and Y. Amemiya (The Univ. of Tokyo, CREST, JST)

References

[1] Y. Okumura and K. Ito, *Advanced Materials* **13** (2001) 485.
[2] J. Bastide and L. Leibler, *Macromolecules* **21** (1988) 2647.
[3] T. Karino, Y. Okumura, C. M. Zhao, T. Kataoka, K. Ito and M. Shibayama, *Macromolecules* **38** (2005) 6161.

2-7 XAS Study of the Electronic Structure of Olivine-Type Phosphate for Li-Ion Batteries

Due to their high electrical density Li-ion secondary batteries have come to be widely used in consumer electronic devices such as cellular phones and personal computers. $LiMPO_4$ phosphate systems (where M represents Fe, Ni or Co), have olivine-related structures, and have recently been intensively studied as candidates for positive electrodes. In olivine-type phosphates it has come to be generally recognized that PO_4 polyanion units form their valence and conduction bands far from the Fermi level where electronic exchange mainly occurs, due to their having a closed-shell electronic configuration. As a result, the transition-metal valence electrons tend to be isolated from those of the polyanions, leading to the fact that the electronic exchange arising from Li removal/uptake mainly occurs at the transition-metal ions. It is expected that this isolated transition-metal electronic structure is the reason for the observed high-voltage properties, and also leads to low electronic conductivity, causing technical difficulties in the fabrication of batteries. Thus an understanding of this unique electronic structure is important if the system is to be applied to rechargeable lithium-ion batteries.

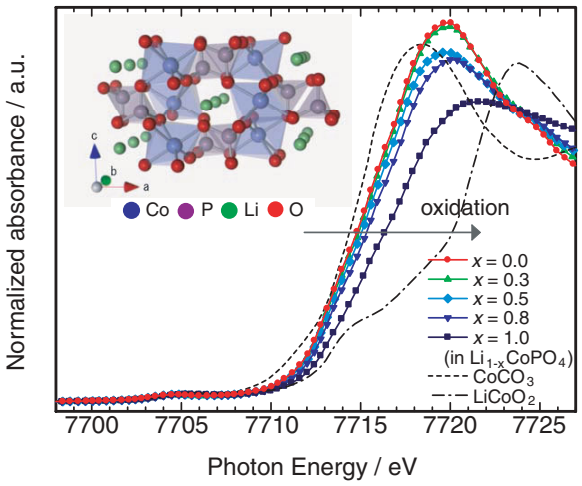

Figure 16
Co K-edge XAS in $Li_{1-x}CoPO_4$ recorded during the lithium extraction process. The inset shows the crystal structure of olivine-type $LiCoPO_4$.

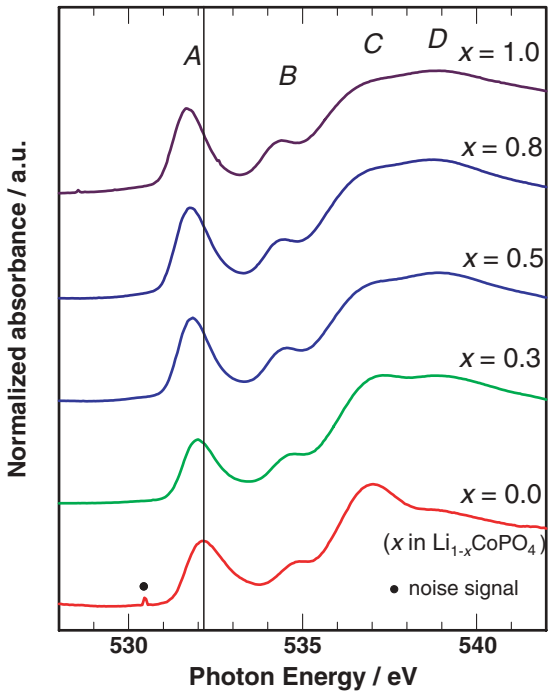

Figure 17
O K-edge XAS of $Li_{1-x}CoPO_4$ recorded during the lithium extraction process.

Co, P, and O K-edge XAS studies were carried out using synchrotron radiation at beam lines BL-7C, BL-11B, and BL-11A [1,2]. Figure 16 shows the Co K-edge XANES recorded around the threshold energy for electrochemically prepared $Li_{1-x}CoPO_4$ samples. Since the threshold energy of $LiCoPO_4$ is close to that of the divalent reference sample $CoCO_3$, the Co ions in $LiCoPO_4$ are expected to be almost divalent. The threshold energy gradually shifts to higher energies with charge reaction, indicating that the Co ions are oxidized for charge compensation over the entire region of the charge reaction (from $x = 0.0$ to 1.0). The absorption peak in the P K-edge XANES spectra gradually shifts with electrochemical Li removal, resulting in an ≈ 0.2 eV shift at a composition of $x = 1.0$. This indicates that the phosphate ions also contribute to the variation of the electronic structure and become less negative with charging.

The results of the O K-edge XANES study of $Li_{1-x}CoPO_4$ are shown in Fig. 17. Sharp absorption peaks appear in the lower energy region. Since they are caused by transitions to unoccupied states formed from the Co 3*d*-O 2*p* hybridized orbitals, peak A is attributed to absorption associated with the Co 3*d* - O 2*p* hybridized orbital. Peak A gradually shifts to lower energies at small *x* values ($0 \leqq x \leqq$ approx. 0.5). The intensity of peak A increases with composition *x*, indicating an increase of holes at oxygen sites. This peak shift and intensity increase indicate a decrease in *d* electron donation from the transition-metal ions to hybridized orbitals. In addition, only a small variation was observed at the O K-edge XAS in the region of $x \approx 0.5$, a one-to-one correspondence to that observed in the Co K-edge XANES. Therefore, it can be concluded that the oxide oxygen ions only contribute to charge compensation process at an early stage of lithium extraction, while the cobalt ions contribute to it at a later stage of the reaction.

An analysis of the XANES study for $Li_{1-x}CoPO_4$ shows that two effects are responsible for the modification of the electronic structure of the PO_4 polyanion, (1) hybridization between the Co 3*d* and O 2*p* orbitals, and (2) polarization induced by the strong ionic character of the Li ions. The variation in the Co-, P- and O K-edge XANES spectra reveals the important role of the hybridization between the Co and O ions and of the polarization in the Li-O-P sequences.

Y. Uchimoto[1] and Y. Kitajima[2] ([1]Kyoto Univ., [2]KEK-PF)

References

[1] M. Nakayama, S. Goto, Y. Uchimoto, M. Wakihara, Y. Kitajima, T. Miyanaga and I. Watanabe, *J. Phys. Chem. B*, **109** (2005) 11197.
[2] M. Nakayama, S. Goto, Y. Uchimoto, M. Wakihara and Y. Kitajima, *Chemistry of Materials*, **16** (2004) 3399.